Acta Geod Geophys (2015) 50:133–149
DOI 10.1007/s40328-014-0094-0

Constraints on the thickness and seismic properties of the lithosphere in an extensional setting (Nógrád-Gömör Volcanic Field, Northern Pannonian Basin)

R Klébesz · Z Gráczer · Gy Szanyi · N Liptai · I Kovács · L Patkó · Zs Pintér · Gy Falus · V Wesztergom · Cs Szabó

Received: 1 September 2014 / Accepted: 4 December 2014 / Published online: 23 January 2015

Abstract The Nógrád-Gömör Volcanic Field (NGVF) is one of the five mantle xenolith bearing alkaline basalt locations in the Carpathian Pannonian Region. This allows us to constrain the structure and properties (e.g. composition, current deformation state, seismic anisotropy, electrical conductivity) of the upper mantle, including the lithosphere-asthenosphere boundary (LAB) using not only geophysical, but also petrologic and geochemical methods. For this pilot study, eight upper mantle xenoliths have been chosen from Bárna-Nagykő, the southernmost location of the NGVF. The aim of this study is estimating the average seismic properties of the underlying mantle. Based on these estimations, the thickness of the anisotropic layer causing the observed average SKS delay time in the area was modelled considering five lineation and foliation end-member orientations. We conclude that a 142–333 km thick layer is required to explain the observed SKS anisotropy, assuming seismic properties calculated by averaging the properties of the eight xenoliths. It is larger than the thickness of the lithospheric mantle. Therefore, the majority of the delay time accumulates in the sublithospheric mantle. However, it is still in question whether a single anisotropic layer, represented by the studied xenoliths, is responsible for the observed SKS anisotropy,

Electronic supplementary material The online version of this article (doi:10.1007/s40328-014-0094-0) contains supplementary material, which is available to authorized users.

R. Klébesz (✉) · Z. Gráczer · G. Szanyi · V. Wesztergom
Geodetic and Geophysical Institute, MTA Research Centre for Astronomy and Earth Sciences, Sopron 9400, Hungary
e-mail: klebesz.rita@csfk.mta.hu

N. Liptai · L. Patkó · Z. Pintér · C. Szabó
Lithosphere Fluid Research Lab, Department of Petrology and Geochemistry, Eötvös University, Budapest 1117, Hungary

I. Kovács · G. Falus
Geological and Geophysical Institute of Hungary, Budapest 1143, Hungary

Present address:
Z. Pintér
Bayerisches Geoinstitut, University of Bayreuth, 95440 Bayreuth, Germany

as it is assumed beneath the Bakony–Balaton Highland Volcanic Field (Kovács et al. 2012), or the sublithospheric mantle has different layers. In addition, the depths of the Moho and the LAB ($25 \pm 5, 65 \pm 10$ km, respectively) were estimated based on S receiver function analyses of data from three nearby permanent seismological stations.

Keywords Seismic anisotropy · Mantle xenolith · S receiver functions · Lithospheric mantle · LAB · Moho

1 Introduction

Study of the subcontinental lithospheric mantle, in many cases, is only possible trough different geophysical methods (e.g. seismology, magnetotellurics). However, upper mantle rocks occurring at various geodynamical settings can provide direct information about the geochemical composition and deformation history of the lithospheric mantle. Peridotite massifs can be structurally and compositionally altered, due to their obduction and subsequent long exposure time on the surface, whereas mantle xenoliths could be more representative of the upper mantle. Xenoliths can record geochemical and physical events in the lithospheric mantle, such as melting, enrichment and deformation events. In addition, different physical properties (e.g. seismic properties, electrical conductivity) of the mantle beneath a given area can be estimated based on xenoliths, and subsequently, these can be compared to geophysical data. Several examples from the literature (e.g. Baptiste and Tommasi 2014; Bascou et al. 2011; Fullea et al. 2011, 2012; Jones et al. 2013; Kovács et al. 2012) show that this integrated petrologic, geochemical and geophysical approach yields to a better understanding of the structure and composition of the lithospheric mantle.

One way to constrain the structure of the mantle is trough seismic anisotropy studies. The significance of seismic anisotropy studies lies in the relationship between deformation processes and anisotropic structures. Deformation under ductile conditions leads to the development of crystal preferred orientation (CPO) in anisotropic mantle silicates (e.g. olivine, piroxenes). Due to the strong anisotropy of olivine and its large proportion in the mantle, development of CPO at a large scale may be responsible for seismic anisotropy in the upper mantle. Therefore, characterization of the anisotropic structure, by geophysical methods and/or xenolith studies, can provide direct information on the geodynamic processes (e.g. Long and Becker 2010).

In the Carpathian Pannonian region (CPR) Plio–Pleistocene alkali basalts have sampled the upper mantle at five known volcanic fields, bringing xenoliths to the surface (Fig. 1). In the past few decades, these mantle xenoliths have been extensively studied (for reviews see Dobosi et al. 2010; Szabó et al. 2004). Therefore, there is a vast body of knowledge on the composition and geochemical evolution of the lithospheric mantle beneath the CPR. Thus, recent studies have already focused on the deformation state, in addition to the geochemistry, of the lithosphere (Falus et al. 2007, 2008; Hidas et al. 2007; Liptai et al. 2013). Kovács et al. (2012) recognized that syntheses of petrologic, geochemical, geophysical and structural geological data is essential to constrain the geodynamical history of the CPR.

The aim of this study is to contribute to our existing knowledge of the upper mantle beneath the CPR by using both xenoliths and seismological data. The Nógrád-Gömör Volcanic Filed (NGVF), has been chosen for integrated petrologic, geochemical and geophysical studies. The recent systematical sampling and several ongoing studies of xenoliths in the area, in addition to the three nearby permanent seismological stations, makes the NGVF an excellent target area.

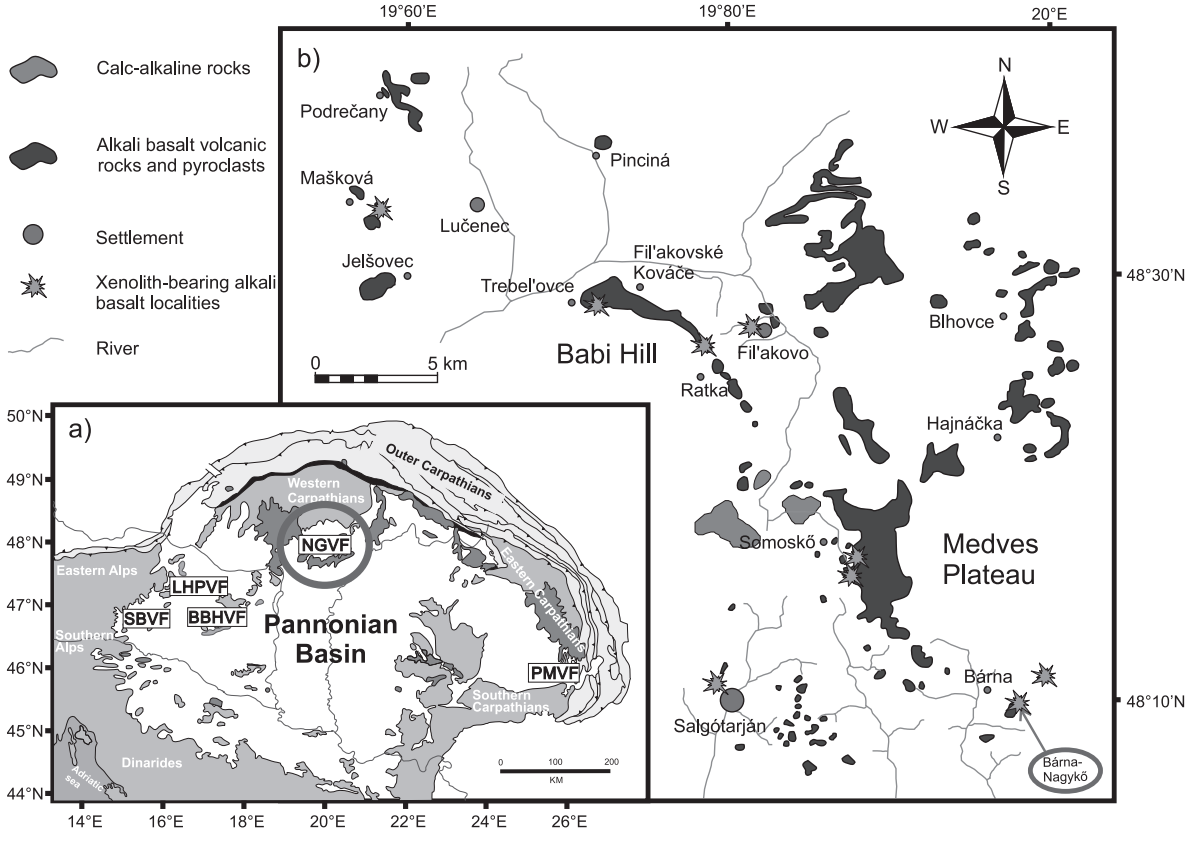

Fig. 1 **a** Location of the mantle xenolith-bearing alkali basalt localities in the CPR (*SBVF* Styrian Basin Volcanic Field, *BBHVF* Bakony-Balaton Highland Volcanic Field, *LHPVF* Little Hungarian Plain Volcanic Field, *NGVF* Nógrád-Gömör Volcanic Field, *PMVF* Persány Mountains Volcanic Field). **b** Location of the upper mantle xenoliths, including the southernmost site, Bárna-Nagykő area within the NGVF

2 Geological settings

The central part of the CPR is the Pannonian Basin, which is characterized by anomalously thin lithosphere. The average thickness of the crust is ~30 km, and the lithosphere-asthenosphere boundary (LAB) is located at 60–100 km in depth (Horváth et al. 2006). The NGVF is located at the northern edge of the Pannonian Basin (Fig. 1). The basement of the NGVF consists of the Gemeric and Veporic units, which consist mostly of Paleozoic and Mesozoic sequences, and sheared and tectonized crystalline nappes (Tomek 1993). In the cover sequence Tertiary sediments and volcanic rocks such as Plio–Pleistocene alkali basalts and their pyroclasts and minor Miocene andesites occur. The alkaline basaltic volcanic centers are dispersed in a NNW-SSE orientation on an approx. 1000 km^2 area from Podrečany (Slovakia) to Bárna (Hungary; Fig. 1).

The formation of the effusive rocks and pyroclasts with basanitic composition is related to post extensional thermal relaxation of the asthenosphere (Embey-Isztin et al. 1993; Harangi 2001; Szabo et al. 1992). The age of the volcanism at this area is 7.2–0.4 Ma, based on K/Ar ages (Balogh et al. 1986; Hurai et al. 2013; Pécskay et al. 2006). Xenoliths are abundant in the volcanics at NGVF along the Podrečany-Bárna zone, however they are absent in the volcanics east of Fil'akovo. Xenoliths reported from the area show large compositional range, such as Cr-diopside suite of ultramafic xenoliths (Konečny et al. 1995; Szabó and Taylor 1994), clinopyroxene-rich xenoliths that are interpreted as cumulates trapped at the mantle-crust boundary (Kovács et al. 2004; Zajacz et al. 2007), and few lower crustal granulite xenoliths (Kovács and Szabó 2005). This paper focuses on peridotite xenoliths from Bárna-Nagykő location, which is in the southern part of the NGVF (Fig 1).

3 Sample descriptions

For this study, 8 lherzolite xenoliths have been used. These xenoliths are part of a larger collection and they were chosen as representative samples for electron back scattered diffraction (EBSD) studies during previous studies (Liptai 2013; Liptai et al. 2013; and unpublished data). The main lithological and deformation characteristics of the eight xenoliths relevant for this study, including CPO patterns of olivine and pyroxenes, are summarized here. However, the interpretation of these data is beyond the scope of this paper, it will be presented elsewhere (Liptai et al. submitted).

The peridotites are lherzolites, composed of olivine (70–88 vol%), orthopyroxene (5–16 vol%), clinopyroxene (5–13 vol%) ± spinel (≤1 vol%, Table 1). Three of the xenoliths of this study (NBN032A, NBN0311, NBN0321) have porphyroclastic texture (Table 1). The porphyroclasts are dominantly orthopyroxenes with curvilinear grain boundaries and sizes between 1.0–5.3 mm, whereas the neoblasts (i.e., olivine, orthopyroxene and clinopyroxene) are usually ≤0.6 mm (Liptai et al. 2013) and have polygonal shapes with straight boundaries. The other five xenoliths (NBN035, NBN0316, NBN0319, NBN9, NBN27) have equigranular texture (Table 1), with the typical grain size ≤1.2 mm (Liptai et al. 2013; Szabó and Taylor 1994). Olivine grains often show undulose extinction and low-angle subgrain walls. Melt pockets, consisting of glass and secondary minerals (spinel and clinopyroxene), are also present; Liptai et al. (2013) interpret these features as a result of increasing temperature in the deep prior to sampling.

Silicate minerals in the studied samples do not show visible elongation, thus lineation and foliation is defined by shape and position of spinel grains and melt pockets. For samples where lineation and foliation is observable (NBN032A, NBN0311, NBN0321, NBN035,

Table 1 Texture, modal composition (ol—olivine, opx—orthopyroxene, cpx—clinopyroxene, sp—spinel), rock type, CPO symmetry type, J index and seismic properties (Vp—P wave velocity, AVs—shear waves polarization anisotropy, Vs1—velocity of the faster shear wave, Vs2—velocity of the slower shear wave, dVs—difference of the faster and slower shear wave, Vp/Vs1—ratio of the velocities of the P wave and the slower shear wave, Vp/Vs2—ratio of the velocities of the P wave and the faster shear wave) of the 8 peridotite xenoliths from the study area (Bárna-Nagykő, Nógrád-Gömör Volcnic Field)

Sample	Texture	Modal composition				Rock type	CPO type	J index	Vp			AVs		Vs1		
		Ol	Opx	Cpx	Sp				km/h		%	%		km/h		%
									max	min	A	max	min	max	min	A
NBN-9	Equigranular	87	5	8		Lherzolite	A-type	3.44	8.55	8.06	5.80	4.28	0.15	4.94	4.78	3.50
NBN-27	Equigranular	83	9	8		Lherzolite	A-type	3.18	8.61	8.04	6.90	5.31	0.19	4.97	4.80	3.60
NBN032A	Porphyroclastic	88	5	5	1	Lherzolite	A-type	2.61	8.60	8.06	6.60	4.45	0.08	4.95	4.81	2.80
NBN035	Equigranular	79	15	6	0	Lherzolite	D-type	2.64	8.55	8.08	5.60	4.00	0.14	4.94	4.81	2.70
NBN0311	Porphyroclastic	81	7	10	1	Lherzolite	A-type	3.39	8.51	8.00	6.10	4.42	0.08	4.96	4.78	3.70
NBN0316	Equigranular	79	11	9	1	Lherzolite	D-type	2.44	8.52	8.15	4.50	3.18	0.08	4.90	4.83	1.40
NBN0319	Equigranular	70	16	13	1	Lherzolite	D-type	2.52	8.51	8.13	4.60	2.92	0.04	4.88	4.85	0.70
NBN0321	Porphyroclastic	84	7	8	1	Lherzolite	A-type	3.56	8.54	8.05	6.00	4.96	0.10	4.96	4.77	4.00

Sample	Vs2			dVs		Vp/Vs1			Vp/Vs2		
	km/h		%					%			%
	max	min	A	max	min	max	min	A	max	min	A
NBN-9	4.82	4.72	2.20	0.21	0.01	1.74	1.68	3.40	1.79	1.71	4.80
NBN-27	4.86	4.70	3.40	0.26	0.01	1.76	1.66	5.50	1.80	1.71	4.90
NBN032A	4.83	4.71	2.50	0.22	0.00	1.75	1.67	4.80	1.79	1.71	4.50
NBN035	4.85	4.72	2.70	0.19	0.01	1.74	1.67	3.80	1.78	1.71	4.00
NBN0311	4.80	4.72	1.60	0.21	0.00	1.74	1.67	3.90	1.78	1.69	5.30
NBN0316	4.86	4.73	2.60	0.15	0.00	1.75	1.68	3.90	1.76	1.72	2.50
NBN0319	4.86	4.73	2.60	0.14	0.00	1.75	1.68	4.20	1.75	1.72	2.30
NBN0321	4.82	4.72	2.10	0.24	0.01	1.73	1.68	2.90	1.79	1.70	5.40

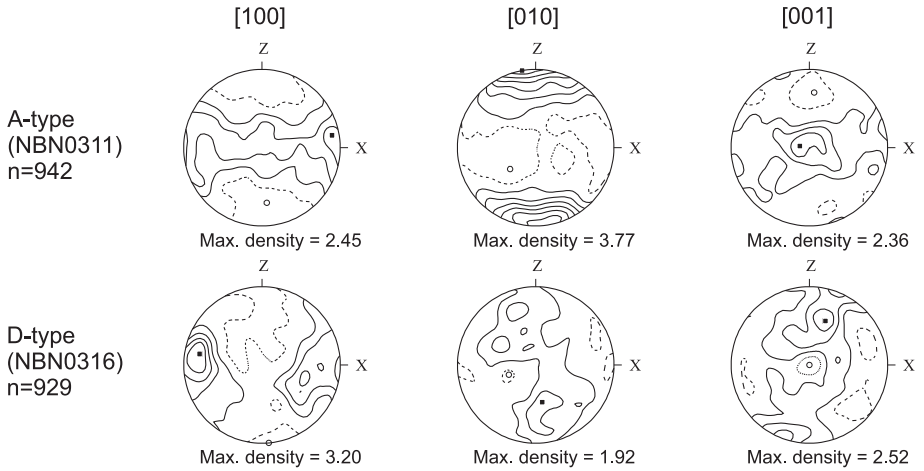

Fig. 2 Pole figures of typical A- and D-type olivine CPO in the studied xenoliths, pictured in lower hemisphere equal area projections. Contours are 0.5 multiples of uniform distribution, lowest value contour is marked with a dashed line. *Black square* and *white circle* represent maximum and minimum axis densities, respectively, and n stands for the number of measured grains

NBN0316, NBN0319) thin sections were prepared parallel to the xz-plane (x is parallel to the lineation and z is normal to the foliation). Since these xenoliths have olivine [100] and [010] maxima parallel to x and z, respectively, samples in which lineation and/or foliation was not observable (NBN9, NBN27) were rotated so that olivine axes match the directions mentioned above.

Olivine [100] and [010] axes in the three porphyroclastic and two equigranular (NBN9, NBN27) textured xenoliths have clear maxima parallel to the lineation and normal to the foliation, respectively; with [010] usually showing higher maximum densities and [100] depicting girdle-like distribution in the plane of foliation. [001] axes are generally more scattered (Fig. 2). This CPO type is recognized as A-type orientation (e.g., Jung et al. 2006; Kovács et al. 2012). In case of the other three equigranular xenoliths (NBN035, NBN0316, NBN0319) olivine [100] axes display clear maxima parallel to the lineation, whereas [010] and [001] axes distribute in a girdle in a plane normal to the lineation (Fig. 2), which is referred to as D-type CPO (Jung et al. 2006). Orthopyroxene and clinopyroxene crystal axes show scattered distribution with occasional maxima at random angles, which is attributed to overrepresentation of certain grains due to incomplete indexation during EBSD analyses resulting in recording as multiple grains with similar orientation.

Strength of fabric is quantified by the J-index (Bunge 1982), which is a dimensionless index ranging between 1 (for random orientation) and infinity (for single crystal). J-indices of the studied xenoliths range from 2.44 to 3.56.

4 Previous studies of seismic anisotropy in the CPR

Seismic anisotropy is commonly studied by the measurements of shear wave splitting using SKS phases. It can constrain the orientation of the fast polarization direction, which is usually believed to be parallel to the mantle flow direction, and the strength and geometry of the anisotropic structure. However, it does not tell much about the depth distribution of anisotropy (for review, see Long and Becker 2010 and references therein).

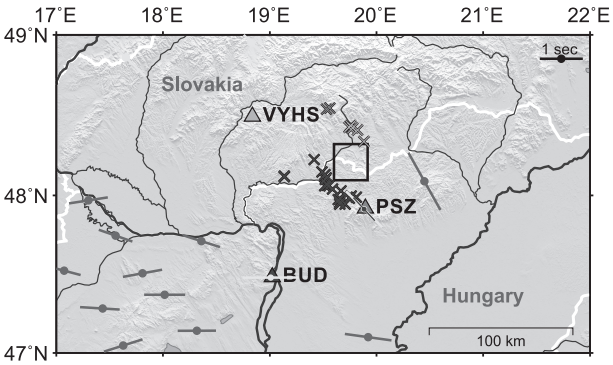

Fig. 3 Location of the seismological stations (*triangles*) used in this study and the distribution of piercing points (*crosses*) of S receiver functions for 70 km depth. The color of the piercing points indicates the corresponding station. Operating organizations of the seismological stations: BUD—MTA CSFK Geodetic and Geophysical Institute, Hungary; PSZ—GEOFON Global Seismic Network, GFZ, Germany & MTA CSFK Geodetic and Geophysical Institute, Hungary; VYHS—Geophysical Institute, Slovak Academy of Sciences, Slovakia. Magnitude and direction of fast polarization direction of the near vertically propagating SKS phase are also shown. Data from (i) *red*—Dando et al. 2011; Kovács et al. 2012; Stuart et al. 2007; (ii) *yellow*—Kovács et al. 2012; Stuart et al. 2007; (iii) *blue*—Ivan et al. 2002

Shear wave splitting studies in the CPR concentrated mostly on the western part of the Pannonian Basin and along the Carpathians. Ivan et al. (2008) estimated ∼1.2 s mean delay time of the slow wave and fast directions around 135° for stations in the proximity of the Carpathians. Ivan et al. (2002) calculated 141° and 133° fastest split wave direction and 0.62 and 0.73 s delay times using two different codes at the station PSZ (GE) (Fig. 2). Dricker et al. (1999) estimated fast directions ∼130° and 1.5 s in and near the Carpathians. Stuart et al. (2007) and Kovács et al. (2012) estimated delay times between 0.5 and 1.5 s and observed NW-SE and E-W anisotropy orientations in the CPR and its surrounding area (Fig. 3). In some cases (e.g. Ivan et al. 2002, 2008) the source of the SKS splitting cannot be clearly identified, however due to the similarities in the anisotropy orientations observed within the CPR, and the lack of correlation between the delay times and crustal/lithospheric thickness (Dricker et al. 1999) and shear wave anisotropies calculated based on xenoliths (Kovács et al. 2012) indicate that the anisotropy is not limited only to the lithosphere, but the asthenosphere also should have a major contribution to it.

5 Methods

5.1 S receiver function analysis

S receiver function (SRF) method utilizes steeply incident teleseismic S to P converted waves to constrain the velocity structure beneath the recoding site (e.g., Farra and Vinnik 2000; Yuan et al. 2006). Wave conversion occurs at velocity discontinuities such as the Moho and the LAB. The components are rotated to theoretical radial and tangential directions (LQT local ray coordinate system). As a result P waves dominate the L component, vertically polarized S waves (SV) can be found on the Q component and horizontally polarized waves (SH) on the T component. SRFs are computed by deconvolving the S waveform on the Q component from the corresponding L and T components. Individual SRFs with common piercing points are summed to improve signal-to-noise ratio. Interfaces appear as peaks on the summed SRFs, at times related to their depth.

Using the data of three seismological stations (Fig. 3) the Moho and the LAB depths beneath the study area were investigated with SRFs. Seismograms of earthquakes with magnitude (mb) larger than 5.7 occurred between 2006 and 2013 have been collected for the stations BUD, PSZ and VYHS based on the focal parameters provided by the ANSS Comprehensive Catalog (http://earthquake.usgs.gov/earthquakes/search/). We calculated the piercing points for each station for a reference depth of 70 km. The receiver functions belonging to the piercing points which lie near to the study area were selected and summed (Fig. 3).

SRF calculations (e.g. Farra and Vinnik 2000) were carried out for events with epicentral distances between 60° and 85°. A time window of 150 s in length was selected (100 s before the S wave arrival time and 50 s after it) and the data were bandpass filtered between 4 and 20 s. The ZNE components were rotated to local LQT ray coordinate system, where the rotation was performed using the theoretical backazimuth value and the incidence angle was determined by the method of Kumar et al. (2006). The individual SRFs were moveout corrected for a reference slowness of 6.4 s/° based on the IASP91 velocity model (Kennett and Engdahl 1991). In order to make the SRF comparable to the P wave receiver functions, the polarity and time axis of the SRFs were reversed, thus the positive values of the receiver functions indicate interfaces of increasing velocity with depth and vice versa.

5.2 Calculation of seismic properties based on CPO measurements

Seismic properties and their 3D distribution of the Bárna-Nagykő lherzolite xenoliths were calculated based on the olivine, orthopyroxene, clinopyroxene CPO, and on the modal composition (Mainprice 1990). The CPO were measured by EBSD at University of Montpellier II (Montpellier, France), using a JEOL JSM-5600 scanning electron microscope equipped with an EBSD system, producing crystal orientation maps, which covered the entire thin section. Modal composition of the xenoliths was determined based on the phase maps of the thin sections obtained during the EBSD analyses. For details of the EBSD data acquisition and treatment, see e.g. Falus et al. (2008). For olivine, orthopyroxene and clinopyroxene, the single crystal elastic tensors of Abramson et al. (1997), Jackson et al. (2007) and Isaak et al. (2006) at ambient conditions were used. A Voigt-Reuss-Hill averaging was applied in all calculations. The calculated seismic properties of all eight xenoliths are summarized in Table 1.

The average seismic properties of the mantle beneath the southern part of the NGVF were estimated by averaging the calculated elastic tensors of each xenolith. By using this approach, we assume that the orientation of the foliation and lineation is the same for all samples, therefore, it will result in an upper bound for the estimated anisotropy. By using all xenoliths with equal weight in averaging, we also assume that these lherzolite samples accurately represent the lithospheric mantle. However, considering published results (Liptai et al. 2013; Szabó and Taylor 1994), and unpublished xenoliths, we conclude that about 20 % of all samples have secondary recrystallized texture that are not considered in this study due to the lack of EBSD data. The amount of uncertainty this assumption introduces, though, cannot be determined and is neglected in this study.

6 Results

6.1 SRF

In the resulting SRF two significant, large amplitude phases can be seen at 3.2 s and at 7.6 s (Fig. 4). The first, positive peak corresponds to the Moho, whereas the second, negative peak

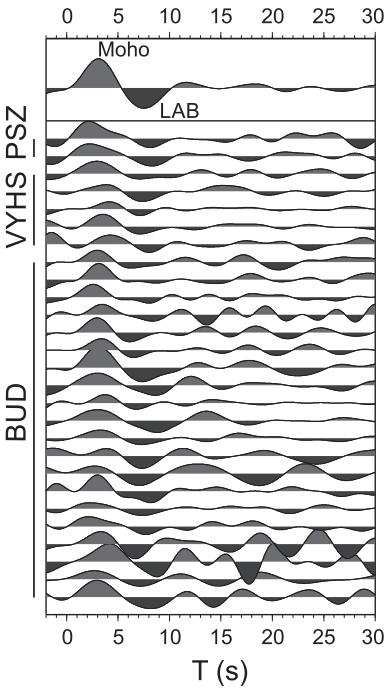

Fig. 4 Individual moveout corrected S receiver functions (*lower panel*) belonging to the piercing points displayed in Fig. 2 and their sum (*upper panel*). Two significant peaks (a positive and a negative) can be clearly observed. They correspond to the S-to-P conversions at the Moho and at the LAB, respectively

is related to the LAB. Based on the IASP91 model (Kennett and Engdahl 1991), the depth of the Moho and the LAB can be estimated as 25 ($\pm$5) km and 65 ($\pm$10) km, respectively. The estimated errors take into account the effects of 5 % variation of seismic velocity for the IASP91 model in the crust and some additional errors due to lateral heterogenities and noise (Mohammadi et al. 2013).

6.2 Seismic anisotropy

Olivine CPO symmetry patterns and 3D distribution of the calculated seismic properties are reported in Table 1 and in the online resource. The 3D distribution of the average seismic properties calculated based on the eight xenoliths of this study is also reported in Table 1, and shown in Fig. 5. All xenoliths, including the average, have seismic anisotropy patterns with some similar characteristics. The fastest P wave direction is always aligned with the olivine [100] axis maxima, which corresponds to the lineation. The fast S (S1) wave polarization planes all include the lineation and therefore, the projection of the S1 polaritation direction on the surface will be parallel to the lineation, which marks the fossil flow direction. S1 wave velocity is minimum for waves propagating at high angles ($\geq$60°) to the lineation and the foliation, and the highest at $\sim$45° to the lineation in the foliation plane, except in xenolith NBN0321, where it is highest normal to the lineation in the foliation plane. The Vp/Vs1 ratios are the highest for waves propagating at low angle ($\leq$30°) to the lineation and low for waves propagating at high angles ($\geq\sim$ 45°) to the lineation. In some cases the minimum can be identified for propagation directions normal or close to normal to both the lineation and the foliation. The Vp/Vs2 ratios are the highest for waves propagating in the foliation plane, in most cases a clear maximum is observed parallel to the lineation and low velocities at $\geq$60° to the foliation.

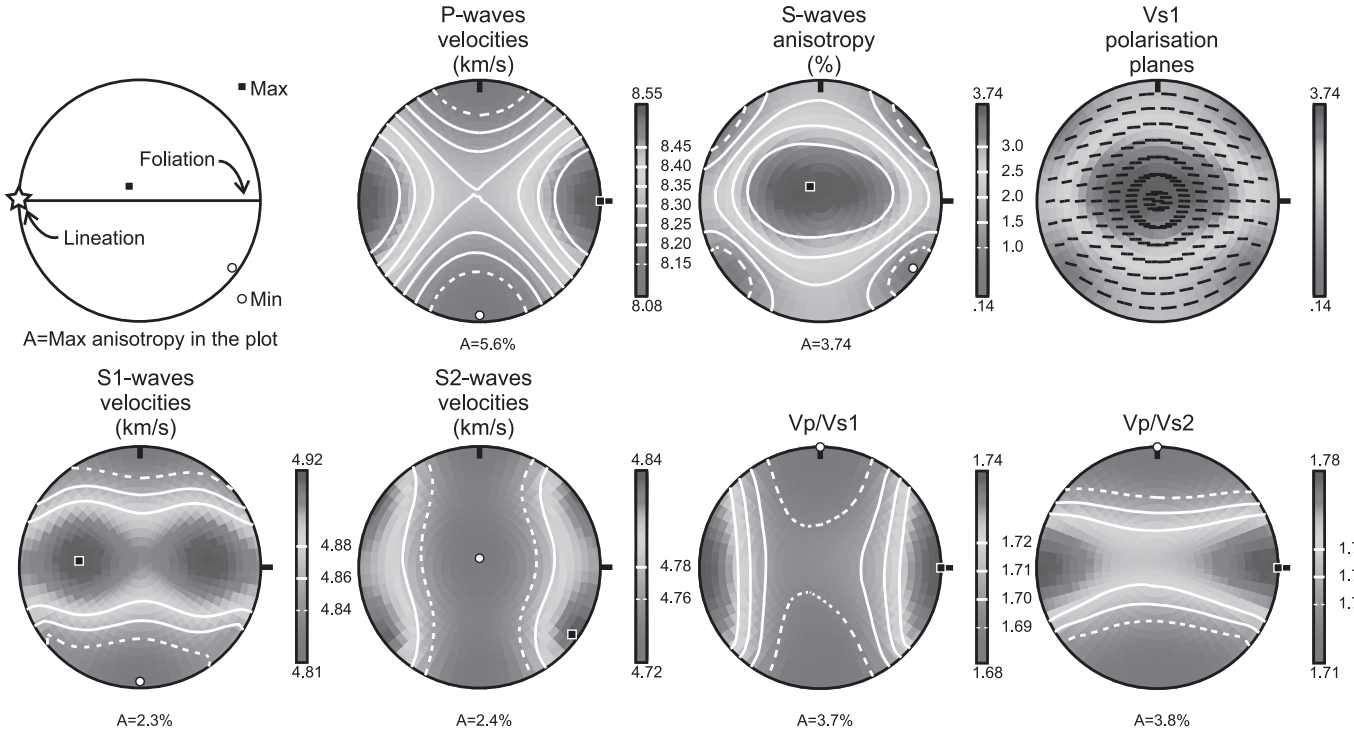

Fig. 5 Seismic properties of the average sample obtained by averaging the elastic tensors of the 8 studied peridotite xenoliths. From *left* to *right* and *top* to *bottom*, schematic representation of the lineation and foliation reference frame used in this study, variation as a function of the propagation direction of the P wave velocities (Vp in km/s), of the shear wave polarization anisotropy [AVs in $\% = 200 \times (Vs1 - Vs2) / (Vs1 + Vs2)$], of the polarization of the fast shear wave S1 (coloring represent the intensity of AVs, as in the previous plot), of the two quasi-shear waves (Vs1 and Vs2) velocities, and of the Vp/Vs1 and Vp/Vs2 ratios. Lower hemisphere stereographic projections

The changes in olivine CPO symmetry cause small variations in the seismic anisotropy patterns. The lherzolite xenoliths displaying A-type olivine CPO pattern and xenolith NBN035 show a distinct Vp minimum at normal or close to normal to the foliation. S wave anosotropy is minimum at 45° to both the lineation and the foliation and it is the highest at ∼45° to the lineation in the foliation plane. S2 wave velocity in case of xenoliths displaying A-type fabric is minimum for waves that are propagating normal to the lineation in and perpendicular to the foliation, and the highest at ∼45° to the lineation and the foliation plane, except in xenolith NBN032A.

Xenoliths NBN 0316 and NBN0319 (D-type) do not show a clear Vp minimum, P wave velocity is low at every direction normal to the lineation. In case of all D-type xenoliths and NBN032A, S wave anisotropy is minimum for waves propagating at low angle to the lineation and the highest normal to the lineation in the foliation plane. S2 wave velocity is low for waves propagating normal or close to normal to the lineation and the highest at low angles ($\leq 30°$) to the lineation.

The average sample show patterns intermediate between the two types described above. The P wave velocity pattern is similar to those with A-type olivine CPO symmetry, in contrast S2 wave velocity pattern resembles to those with D-type olivine CPO symmetry. S wave anisotropy is minimum at 45° to both the lineation and the foliation, like for xenoliths with A-type symmetry, but it is highest normal to the lineation in the foliation plane as it is for xenoliths with D-type symmetry.

No wide variations in seismic properties of the individual samples were observed, the main variation is in the intensity of the anisotropy (Table 1). A clear linear correlation between the J-index and the maximum anisotropies (P wave and S1 wave anisotropy and S wave splitting) was not recognized, xenoliths with higher J-index, though, tend to have stronger anisotropy (Table 1).

7 Discussion

7.1 Estimated Moho and LAB depths

The crustal and lithospheric thickness maps of the CPR constructed by Horváth et al. (2006) is generally accepted, therefore we compared our results to these maps in order to evaluate them. These maps are the improved versions of the maps of Horváth (1993). The crustal thickness map is based on data obtained by traditional refraction methods, reflection seismic profiling and gravity modelling studies (Horváth 1993; Horváth et al. 2006). Based on these maps the estimated depth of the Moho beneath the NGVF is ∼27.5 km, which is in agreement with the results of recent deep crustal seismic profiling (Grad 2006; Hrubcová et al. 2010; Tomek 1993) and the result of this study within the estimated error.

The crustal thickness is well constrained in the CPR, however, significantly less data is available on the lithospheric thickness. The lithospheric thickness map of Horváth (1993) was constructed based on P wave travel time residuals and magnetotelluric soundings, and it estimates the LAB at 60–80 km in depth beneath the NGVF. However, the lithospheric thickness map of Horváth et al. (2006), which was improved by new magnetotelluric results, estimates the LAB at greater depth (80–100 km) beneath the study area. Our result (65 ± 10 km) is in good agreement with the result of Horváth (1993), however it indicates a shallower LAB than the currently generally accepted values of Horváth et al. (2006). Plomerová and Babuška (2010) presented a uniform updated model of the European LAB based on P wave residuals. They predict an even deeper LAB beneath the NGVF, at least 100 (± 10) km.

Geissler et al. (2010) used SRF obtained at 78 European permanent broad-band stations to estimate the thickness of the European lithosphere. Most of the Sp piercing points for an 80 km deep LAB were located ~80 km N-E from the stations in the study of Geissler et al. (2010). The NGVF is in the proximity of the Sp piercing points of the BUD station, therefore we assume that the BUD station can be used for comparison. Geissler et al. (2010) estimated 74 km for LAB depth and 28 km for Moho depths based on the data obtained at the BUD station, which is in good agreement with our result within the estimated errors.

Jones et al. (2010) pointed out that there can be significant differences in the estimated LAB depths based on the method used (i.e. magnetotellurics, SRF, analysis of P travel time residuals). Our results are similar to those obtained by the same method, i.e. SRF (Geissler et al. 2010). The differences between our estimated depths and the previously published lithospheric maps (Horváth 1993; Horváth et al. 2006; Plomerová and Babuška 2010) might only be due to the used methods and data based on which the maps were constructed.

Another possible way of evaluating the estimated depths is to compare them to the estimated originating depths of the xenoliths from the NGVF. The originating depth of the xenoliths can be estimated based on the calculated equilibrium temperature and the appropriate heat flow values of the area, with an uncertainty of ±12 km (Kovács et al. 2012). Liptai et al. (submitted) estimated that the xenoliths from Bárna-Nagykő are from 30–35 km, whereas xenoliths from the central part (Babi Hill and Medves Plateau) of the NGVF (Fig 1.) are from ~40–50 km. However, they argue, that incipient melting preserved in the xenoliths might have caused a compositional change in the pyroxene. Consequently, the estimated equilibrium temperatures, and hence the originating depth, can only be considered as a minimum estimate. The originating depth range of the xenoliths, considering also the uncertainty of the estimation and possible underestimation, is within our estimated range of the lithospheric mantle (between 25 ± 5 and 65 ± 10 km in depth).

7.2 Seismic anisotropy

The original, in-situ orientation of the xenoliths is unknown due to their transport to the surface, therefore we are unable to constrain the orientation of the foliation and lineation in the anisotropic layer. However, we are able to estimate the thickness of the anisotropic structure that could cause the observed delay times (e.g. Baptiste and Tommasi 2014; Ben-Ismail et al. 2001; Kovács et al. 2012; Michibayashi et al. 2006; Pera et al. 2003). The thickness (T) of an anisotropic layer is given by Eq. (1), where dt is the delay time of SV, ⟨Vs⟩ is the average velocity of the fast and slow velocities, and AVs is the anisotropy for a specific propagation direction expressed as a percentage (e.g. Pera et al. 2003).

$$T = 100dt \cdot \frac{\langle Vs \rangle}{AVs} \tag{1}$$

Ignoring the potential effect of crustal anisotropy (such as in e.g. Kovács et al. 2012), the calculated seismic properties of the average mantle beneath Bárna-Nagykő (Fig. 4 and Table 1) was used to estimate the thickness of the anisotropic layer. Five end-member orientations (Fig. 6) were considered for these estimations, following the example of Baptiste and Tommasi (2014), such as horizontal foliation and lineation (case 1), vertical foliation but horizontal lineation (case 2), vertical foliation and lineation (case 3), 45° dipping foliation and lineation (case 4), 45° dipping foliation and horizontal lineation (case 5). Model calculations were carried out for two different scenarios with two different dt for all five end-member orientations. In the first scenario, we assumed ~1.1 s by considering all observations of the CPR (Dricker et al. 1999; Ivan et al. 2002, 2008; Kovács et al. 2012; Stuart et al. 2007), in

		Avs (%)	T (km) dt=1.1 s	T (km) dt=1.3 s	T (km) BBHVF (dt=1 s)
Case 1	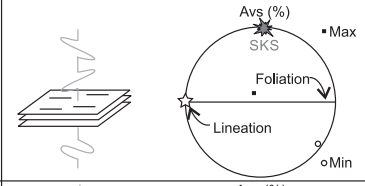	1.88	282	333	123
Case 2	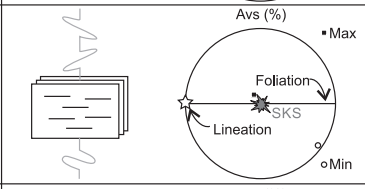	3.74	142	168	85
Case 3	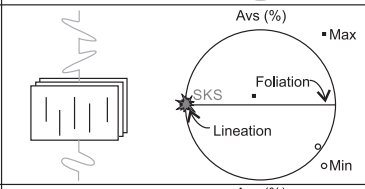	2	265	313	196
Case 4	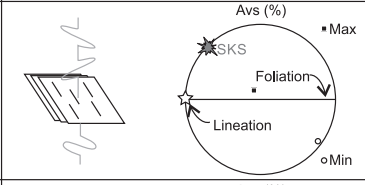	0.5	1061	1254	140
Case 5	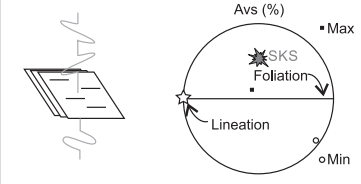	2.75	193	228	109

Fig. 6 Calculated SKS anisotropy for the five different end-member orientations of the foliation and the lineation: (Case 1) horizontal foliation and lineation, (Case 2) vertical foliation with a horizontal lineation, (Case 3) vertical foliation and lineation, (Case 4) 45° dipping foliation and lineation, and (Case 5) 45° dipping foliation with a horizontal lineation, after Baptiste and Tommasi 2014. Estimated thickness (T) of the anisotropic layer in case of dt = 1.1 s and dt = 1.3 s, and in case of Bakony-Balaton Highland Volcanic Field (BBHVF) (assuming dt = 1 s)

the second we assumed ~1.3 s based on the observed delay times at the three seismological stations closest to the NGVF (data from: Piszkéstető - Ivan et al. 2002; and Piszkéstető, Bükk Mts., Central Slovakia in Fig. 2; data from Kovács et al. 2012).

For the five end-members the S wave polarization anisotropy is 1.88, 3.74, 2.0, 0.5 and 2.75 % for case 1–5, respectively. The average S wave velocity is 4.82 km/s. Hence, the estimated thickness of the anisotropic structure is 282, 142, 265, 1061 and 193 km, and 333, 168, 313, 1254 and 228 km for case 1–5, considering dt = 1.1 s then 1.3 s, respectively (Fig. 6). Case 1 and 3 gives similar results, whereas case 2 and 5 requires thinner, case 4 requires much thicker anisotropic layer to produce the same delay time. Based on global datasets, depth dependent of

anisotropy in the upper mantle was recognized (Kustowski et al. 2008; Long and Becker 2010; Wenk 2004). The global average upper mantle anisotropy is significant in the upper ~200–250 km, and then gradually weakens between 250–400 km (Kustowski et al. 2008; Long and Becker 2010). Therefore, assuming that a single anisotropic layer causes the observed delay time, we can conclude that only case 4, a layer with foliation and lineation close to 45°, is unlikely considering the global average upper mantle anisotropy. Without further seismic evidence, however, it is not possible to determine the orientation of the lineation and the foliation, but in the other four cases a 142–282 or 168–333 km thick layer is needed to produce the observed delay times. These thicknesses are significantly greater than the estimated lithospheric mantle thickness (~40 km), therefore at least ~100 km thick sublithospheric mantle is required with the same structure to account for the seismic observations.

Our results are compared to the thickness of the anisotropic layer beneath the Bakony-Balaton Highland Volcanic Field (BBHVF), in order to see if there is any resemblance between the NGVF and the BBHVF, which is the closest area where similar studies has been carried out (Kovács et al. 2012), and the BBHVF is also the part of the same tectonic unit (ALCAPA). The thickness of the anisotropic layer beneath the BBHVF was recalculated by using Eq. (1) based on the A-type xenolith reported by Kovács et al. (2012), considering the five end-member orientations described above. In the calculations, ~1 s surface delay time was assumed, which was measured at the proximity of BBHVF sites (Kovács et al. 2012). The thickness of anisotropic layer is 123, 85, 196, 140, 109 km for cases 1–5, respectively. The minimum thickness (85 km) is observed in case of vertical foliation and horizontal lineation (case 2), similarly to the estimates for the NGVF. The thickness of the sublithospheric part of the anisotropic layer is ~60–160 km, assuming a ~35 km thick lithospheric mantle, which was estimated beneath the BBHVF (Kovács et al. 2012 and references therein). This thickness (~60–160 km) is considerably smaller than the thickness of the sublithospheric part of the anisotropic layer beneath the NGVF (~100–240 or ~130–290 km), assuming a single anisotropic layer.

In the BBHVF there is compelling evidence that the A-type xenoliths derive from the upper part of a mantle domain which represents asthenospheric material, lithospherized after the Miocene extension (Kovács et al. 2012). Therefore it is reasonable to assume that a single anisotropic layer, sampled by the A-type xenoliths, is responsible for the observed SKS delay times. However, based on the data presented here, it is not yet possible to assess whether the same scenario is true for the NGVF. Consequently, as a second approach, we assumed that the calculated average mantle represents only the lithospheric mantle. This allow us to calculate, by rearranging Eq. (1), the portion of the delay time that accumulates in the lithospheric mantle. Based on the results of this study and previous data from the literature, 25 km thick crust and 55 km thick lithospheric mantle was assumed. As a results, 0.2, 0.4, 0.2, 0.1 and 0.3 s was calculated for cases 1–5, respectively. Even considering the upper limit of the crustal contribution to the delay time, which is typically 0.1 s per 10 km (Barruol and Mainprice 1993), it has become evident that the majority ($\geq$ 50 %) of the delay time may accumulate in the sublithospheric mantle. Further geochemical and deformation studies will be carried out, which might help us constrain the origin of the lithospheric mantle and its connection with the sublithospheric mantle, and hence the origin of the observed anisotropy.

8 Summary

The NGVF proved to be an excellent area for integrated geophysical and petrologic and geochemical studies. Data from three nearby seismological stations could be used to esti-

mate the depths of the Moho and the LAB ($25 \pm 5, 65 \pm 10$ km, respectively). Mantle xenoliths can be a powerful tool for estimating the 3D distribution of the seismic properties. Relying on these estimated properties and the published SKS delay times, the thickness of the anisotropic structure beneath the NGVF was constrained based on eight mantle xenoliths from the southernmost location, Bárna-Nagykő. The thickness of a single anisotropic structure was estimated at least ∼140 km and maximum ∼330 km. The thickness of the anisotropic structure in case of each foliation and lineation orientations is larger beneath the NGVF than under the BBHVF. This could indicate differences in the anisotropic structures beneath the two area. At this point there is not enough evidence to assume that the delay time accumulates in a single anisotropic layer beneath the NGVF. However, we can conclude that the majority of the delay time accumulates in the sublithospheric mantle. Geochemical studies in the future may give constraints on the link between the lithospheric and sublithospheric mantle, and hence the possible source of the SKS anisotropy.

Acknowledgments The authors thank V. Baptiste for helpful discussion. We are grateful for the thorough review and constructive comments of K. Hidas and an anonymous reviewer. This research was carried out in the framework of the cooperation agreement (TTK/6109/1/2014 and Sz/156/2014) between the Lithosphere Fluid Research Lab at Department of Petrology and Geochemistry of Eötvös University and the Geodetic and Geophysical Institute of the MTA Research Centre for Astronomy and Earth Sciences. This study was partially supported by the TAMOP-4.2.2.C–11/1/KONV-2012-0015 (Earth-system) project sponsored by the EU and European Social Foundation. IK was supported by the Bolyai Postdoctoral Fellowship Program and a Marie Curie International Reintegration Grant (NAMS-230937).

References

Abramson EH, Brown JM, Slutsky LJ, Zaug J (1997) The elastic constants of San Carlos olivine to 17 GPa. J Geophys Res 102:12253–12263. doi:10.1029/97JB00682

Balogh K, Árva-Sós E, Pécskay Z (1986) K/Ar dating of post Sarmatian alkali basaltic rocks in Hungary. Acta Mineral Petrogr Szeged 28:75–93

Baptiste V, Tommasi A (2014) Petrophysical constraints on the seismic properties of the Kaapvaal craton mantle root. Solid Earth 5:45–63. doi:10.5194/se-5-45-2014

Barruol G, Mainprice D (1993) A quantitative evaluation of the contribution of crustal rocks to the shear-wave splitting of teleseismic SKS waves. Phys Earth Planet Inter 78:281–300. doi:10.1016/0031-9201(93)90161-2

Bascou J, Doucet LS, Saumet S, Ionov DA, Ashchepkov IV, Golovin AV (2011) Seismic velocities, anisotropy and deformation in Siberian cratonic mantle: EBSD data on xenoliths from the Udachnaya kimberlite. Earth Planet Sci Lett 304:71–84. doi:10.1016/j.epsl.2011.01.016

Ben-Ismail W, Barruol G, Mainprice D (2001) The Kaapvaal craton seismic anisotropy: petrophysical analyses of upper mantle kimberlite nodules. Geophys Res Lett 28:2497–2500. doi:10.1029/2000GL012419

Bunge HJ (1982) Texture analysis in materials science: mathematical methods. Butterworths, London

Dando BDE, Stuart GW, Houseman GA, Hegedüs E, Brückl E, Radovanovic S (2011) Teleseismic tomography of the mantle in the Carpathian-Pannonian region of central Europe. Geophys J Int 186:11–31. doi:10.1111/j.1365-246X.2011.04998.x

Dobosi G, Jenner G, Embey-Isztin A, Downes H (2010) Cryptic metasomatism in clino- and orthopyroxene in the upper mantle beneath the Pannonian region. In: Coltorti M (ed) Petrological evolution of the European lithospheric mantle: from Archaean to present day, vol special publication 337. Geological Society, London

Dricker I, Vinnik L, Roecker S, Makeyeva L (1999) Upper-mantle flow in eastern Europe. Geophys Res Lett 26:1219–1222. doi:10.1029/1999GL900204

Embey-Isztin A et al (1993) The petrogenesis of Pliocene alkaline volcanic rocks from the Pannonian Basin, Eastern Central Europe. J Petrol 34:317–343

Falus G, Szabo C, Kovacs I, Zajacz Z, Halter W (2007) Symplectite in spinel lherzolite xenoliths from the Little Hungarian Plain, Western Hungary: a key for understanding the complex history of the upper mantle of the Pannonian Basin. Lithos 94:230–247. doi:10.1016/j.lithos.2006.06.017

Falus G, Tommasi A, Ingrin J, Szabó C (2008) Deformation and seismic anisotropy of the lithospheric mantle in the southeastern Carpathians inferred from the study of mantle xenoliths. Earth Planet Sci Lett 272:50–64. doi:10.1016/j.epsl.2008.04.035

Farra V, Vinnik L (2000) Upper mantle stratification by P and S receiver functions. Geophys J Int 141:699–712. doi:10.1046/j.1365-246x.2000.00118.x

Fullea J, Lebedev S, Agius MR, Jones AG, Afonso JC (2012) Lithospheric structure in the Baikal-central Mongolia region from integrated geophysical-petrological inversion of surface-wave data and topographic elevation. Geochem Geophys Geosyst 13:Q0AK09. doi:10.1029/2012GC004138

Fullea J, Muller MR, Jones AG (2011) Electrical conductivity of continental lithospheric mantle from integrated geophysical and petrological modeling: Application to the Kaapvaal Craton and Rehoboth Terrane, southern Africa. J Geophys Res 116:B10202. doi:10.1029/2011JB008544

Geissler WH, Sodoudi F, Kind R (2010) Thickness of the central and eastern European lithosphere as seen by S receiver functions. Geophys J Int 181:604–634. doi:10.1111/j.1365-246X.2010.04548.x

Grad M et al (2006) Lithospheric structure beneath trans-Carpathian transect from Precambrian platform to Pannonian basin: CELEBRATION 2000 seismic profile CEL05. J Geophys Res 111:B03301. doi:10.1029/2005JB003647

Harangi S (2001) Neogene to quaternary volcanism of the Carpathian-Pannonian Region - a review. Acta Geol Hung 44:223–258

Hidas K, Falus G, Szabó C, Szabó PJ, Kovács I, Földes T (2007) Geodynamic implications of flattened tabular equigranular textured peridotites from the Bakony–Balaton Highland Volcanic Field (Western Hungary). J Geodyn 43:484–503

Horváth F (1993) Towards a mechanical model for the formation of the Pannonian basin. Tectonophysics 226:333–357. doi:10.1016/0040-1951(93)90126-5

Horváth F, Bada G, Szafián P, Tari G, Ádám A (2006) Formation and deformation of the Pannonian Basin: constraints from observational data. In: Gee DG, Stephenson R (eds) European lithosphere dynamics, vol memoirs 32. The Geological Society of London, London, pp 191–206

Hrubcová P, Środa P, Grad M, Geissler WH, Guterch A, Vozár J, Hegedűs E (2010) From the Variscan to the Alpine Orogeny: crustal structure of the Bohemian Massif and the Western Carpathians in the light of the SUDETES 2003 seismic data. Geophys J Int 183:611–633. doi:10.1111/j.1365-246X.2010.04766.x

Hurai V, Danišík M, Huraiová M, Paquette J-L, Ádám A (2013) Combined U/Pb and (U-Th)/He geochronometry of basalt maars in Western Carpathians: implications for age of intraplate volcanism and origin of zircon metasomatism. Contrib Miner Petrol 166:1235–1251. doi:10.1007/s00410-013-0922-1

Isaak DG, Ohno I, Lee PC (2006) The elastic constants of monoclinic single-crystal chrome-diopside to 1,300 K. Phys Chem Miner 32:691–699. doi:10.1007/s00269-005-0047-9

Ivan M, Popa M, Ghica D (2008) SKS splitting observed at Romanian broad-band seismic network. Tectonophysics 462:89–98. doi:10.1016/j.tecto.2007.12.015

Ivan M, Tóth L, Kiszely M (2002) SKS Splitting observed at the Hungarian station PSZ - Geofon Network. J Balk Geophys Soc 5:71–76

Jackson JM, Sinogeikin SV, Bass JD (2007) Sound velocities and single-crystal elasticity of orthoenstatite to 1073 K at ambient pressure. Phys Earth Planet Inter 161:1–12. doi:10.1016/j.pepi.2006.11.002

Jones AG, Fishwick S, Evans RL, Muller MR, Fullea J (2013) Velocity-conductivity relations for cratonic lithosphere and their application: example of Southern Africa. Geochem Geophys Geosyst 14:806–827. doi:10.1002/ggge.20075

Jones AG, Plomerova J, Korja T, Sodoudi F, Spakman W (2010) Europe from the bottom up: a statistical examination of the central and northern European lithosphere-asthenosphere boundary from comparing seismological and electromagnetic observations. Lithos 120:14–29. doi:10.1016/j.lithos.2010.07.013

Jung H, Katayama I, Jiang Z, Hiraga T, Karato S (2006) Effect of water and stress on the lattice-preferred orientation of olivine. Tectonophysics 421:1–22. doi:10.1016/j.tecto.2006.02.011

Kennett BLN, Engdahl ER (1991) Traveltimes for global earthquake location and phase identification. Geophys J Int 105:429–465. doi:10.1111/j.1365-246X.1991.tb06724.x

Konečny P, Konečny V, Lexa J, Huraiová M (1995) Mantle xenoliths in alkali basalts of Southern Slovakia. Acta Vulcanol 7:241–247

Kovács I et al (2012) Seismic anisotropy and deformation patterns in upper mantle xenoliths from the central Carpathian-Pannonian region: asthenospheric flow as a driving force for Cenozoic extension and extrusion? Tectonophysics 514–517:168–179

Kovács I, Szabó C (2005) Petrology and geochemistry of granulite xenoliths beneath the Nógrád-Gömör Volcanic Field, Carpathian-Pannonian Region (N-Hungary/S-Slovakia). Miner Petrol 85:269–290

Kovács I, Zajacz Z, Szabó C (2004) Type-II xenoliths and related metasomatism from the Nógrád-Gömör Volcanic Field, Carpathian-Pannonian region (northern Hungary-southern Slovakia). Tectonophysics 393:139–161. doi:10.1016/j.tecto.2004.07.032

Kumar P, Yuan X, Kind R, Ni J (2006) Imaging the colliding Indian and Asian lithospheric plates beneath Tibet. J Geophys Res 111:B06308. doi:10.1029/2005JB003930

Kustowski B, Ekström G, Dziewoński AM (2008) Anisotropic shear-wave velocity structure of the Earth's mantle: a global model. J Geophys Res 113:B06306. doi:10.1029/2007JB005169

Liptai N (2013) Geokémiai jellemvonások és fizikai állapot tanulmányozása nógrád-gömöri felsőköpeny xenolitokon. MSc Thesis, Eötvös University.

Liptai N, Jung H, Park M, Szabó C (2013) Olivine orientation study on upper mantle xenoliths from Bárna-Nagykő, Nógrád-Gömör Volcanic Field (Northern Pannonian Basin, Hungary). Földtani Közlöny 143:371–382 (in Hungarian, with English abstract).

Liptai N, Patkó L, Kovács I, Pintér Z, Hidas K, Tommasi A, Jeffries T, Zajacz Z, Falus G, Szabó C. The upper mantle beneath the Nógrád-Gömör Volcanic Field (Northern Hungary-Southern Slovakia) - an integrated study on spinel lherzolite xenoliths. J Petrol (submitted)

Long MD, Becker TW (2010) Mantle dynamics and seismic anisotropy. Earth Planet Sci Lett 297:341–354. doi:10.1016/j.epsl.2010.06.036

Mainprice D (1990) A FORTRAN program to calculate seismic anisotropy from the lattice preferred orientation of minerals. Comput Geosci 16:385–393. doi:10.1016/0098-3004(90)90072-2

Michibayashi K, Abe N, Okamato A, Satsukawa T, Michikura K (2006) Seismic anisotropy in the uppermost mantle, back-arc region of the northest Japan arc: petrophyisical analyses of Ichinomegata peridotite xenoliths. Geophys Res Lett 33:L10312

Mohammadi N, Sodoudi F, Mohammadi E, Sadidkhouy A (2013) New constraints on lithospheric thickness of the Iranian plateau using converted waves. J Seismol 17:883–895

Pécskay Z et al (2006) Geochronology of Neogene magmatism in the Carpathian arc and intra-Carpathian area. Geol Carpath 57:511–530

Pera E, Mainprice D, Burlini L (2003) Anisotropic seismic properties of the upper mantle beneath the Torre Alfina area (Northern Apennines, Central Italy). Tectonophysics 370:11–30. doi:10.1016/S0040-1951(03)00175-6

Plomerová J, Babuška V (2010) Long memory of mantle lithosphere fabric – European LAB constrained from seismic anisotropy. Lithos 120:131–143. doi:10.1016/j.lithos.2010.01.008

Stuart GW et al. (2007) Understanding extension within a convergent orogen: Initial results from the Carpathian Basins Seismic Project. Eos Trans AGU 88:Fall Meet. Suppl., Abstract S41A–0235

Szabó C, Falus G, Zajacz Z, Kovács I, Bali E (2004) Composition and evolution of lithosphere beneath the Carpathian-Pannonian Region: a review. Tectonophysics 393:119–137

Szabo C, Harangi S, Csontos L (1992) Review of Neogene and Quaternary volcanism of the Carpathian-Pannonian region. Tectonophysics 208:243–256

Szabó C, Taylor LA (1994) Mantle petrology and geochemistry beneath the Nógrád-Gömör Volcanic Field, Carpathian-Pannonian Region. Int Geol Rev 36:328–358

Tomek Č (1993) Deep crustal structure beneath the central and inner West Carpathians. Tectonophysics 226:417–431. doi:10.1016/0040-1951(93)90130-C

Wenk HR (2004) The Texture of rocks in the earth's deep interior: part II. Application of texturing to the deep earth. In: Buschow KHJ, Robert WC, Merton CF, Bernard I, Edward JK, Subhash M, Patrick V (eds) Encyclopedia of materials: science and technology, 2nd edn. Elsevier, Oxford, pp 1–11. doi:10.1016/B0-08-043152-6/01929-X

Yuan X, Kind R, Li X, Wang R (2006) The S receiver functions: synthetics and data example. Geophys J Int 165:555–564

Zajacz Z, Kovacs I, Szabo C, Halter W, Pettke T (2007) Evolution of mafic alkaline melts crystallized in the uppermost lithospheric mantle: a melt inclusion study of olivine-clinopyroxenite xenoliths, northern Hungary. J Petrol 48:853–883. doi:10.1093/petrology/egm004